JPhys Energy

PURPOSE-LED PUBLISHING™

PAPER • OPEN ACCESS

Photovoltaic array design for laser power transmission in space applications

To cite this article: Giovanni Cichelli *et al* 2025 *J. Phys. Energy* **7** 035007

View the article online for updates and enhancements.

You may also like

- 2024 roadmap for sustainable batteries
Magda Titirici, Patrik Johansson, Maria Crespo Ribadeneyra et al.
- Recent status and future prospects of emerging oxygen vacancy-/defect-rich electrode materials: from creation mechanisms to detection/quantification techniques, and their electrochemical performance for rechargeable batteries
Sandeep Kumar Sundriyal and Yogesh Sharma
- Shape engineering and manufacturing of piezoceramics for energy conversion—a review
Guilherme Victor Selicani, Mahmoud Mobin, Vincenzo Esposito et al.

This content was downloaded from IP address 151.64.172.220 on 02/10/2025 at 20:42

Journal of Physics: Energy

PAPER

Photovoltaic array design for laser power transmission in space applications

Giovanni Cichelli[1,*], **Pierluigi Morsaniga**[2], **Giuseppe Gervasio**[2], **Paolo Laporta**[1,3] and **Nicola Coluccelli**[1,3]

[1] Department of Physics, Politecnico di Milano, Piazza Leonardo da Vinci, 32, Milano, 20133, Italy
[2] Thales Alenia Space Italy S.p.A, Strada Antica di Collegno 253, 10146 Torino, Italy
[3] Istituto di Fotonica e Nanotecnologie (IFN), Consiglio Nazionale delle Ricerche, Piazza Leonardo da Vinci, 32, Milano, 20133, Italy
[*] Author to whom any correspondence should be addressed.

E-mail: giovanni.cichelli@polimi.it

Keywords: wireless power transmission, Gaussian beam, photovoltaic

OPEN ACCESS

RECEIVED
28 January 2025

REVISED
25 March 2025

ACCEPTED FOR PUBLICATION
24 April 2025

PUBLISHED
6 May 2025

Original Content from this work may be used under the terms of the Creative Commons Attribution 4.0 licence.

Any further distribution of this work must maintain attribution to the author(s) and the title of the work, journal citation and DOI.

Abstract

Wireless power transmission through lasers can revolutionize energy delivery methods, providing continuous power supply to satellites, unmanned aerial vehicles, and space stations, where traditional power sources are impractical. The receiver uses photovoltaic (PV) cell technology. However, while modern PV panel designs perform well under uniform white-light illumination, such as sunlight, they face limitations when exposed to the non-uniform, typically Gaussian, and highly-monochromatic radiation produced by a laser source. The article focuses on the design of PV panels specifically engineered for power transmission via laser, by taking into account the Gaussian intensity distribution across the panel along with the variations of the electrical parameters due to thermal effects. Two designs are proposed, based on PV cells arrangements in a Ring- or Tree-Shaped geometry, aimed at optimizing energy conversion efficiency, while complying with the mechanical and electrical constraints required by space applications. Numerical simulations predict a maximum conversion efficiency of 37% at an incident laser power of 5 kW and a peak laser intensity of 500 W m^{-2}, approaching the theoretical limit of 42.3% for a single PV cell operated at 1 W cm^{-2}.

1. Introduction

Wireless power transmission (WPT) is increasingly gaining interest in contexts where wiring is either infeasible or entails prohibitively high costs for the entire system to be efficient. Among the various methods of WPT, two prominent technologies have emerged: radio frequency (RF) and laser-based power transmission (LPT). RF power transmission has been extensively studied and implemented due to its capability to cover long distances and to penetrate through various obstacles. This technology leverages electromagnetic waves in the RF spectrum to transmit energy from a source to a receiver, providing a reliable means of power delivery; however, it typically suffers from low energy transfer efficiency and requires large antennas, which can limit its practicality in certain contexts. On the other hand, LPT, also known as laser power beaming, utilizes coherent light beams to transfer energy [1, 2]. This method offers several significant advantages, particularly in the realm of space applications. Laser power beaming provides higher energy densities and improved directionality compared to RF transmission, enabling more precise targeting and reduced energy loss over long distances. These attributes make it an ideal solution for powering satellites, space stations, and other orbital platforms where efficient and focused energy delivery is crucial. More specifically, the high directionality of laser beams is advantageous for maintaining power supply to spacecraft or satellites that are constantly moving and may be located at great distances from the power source [3]; additionally, the compact nature of laser power systems reduces the payload weight and volume on space missions, which is a critical consideration given the high cost of launching materials into orbit. Finally, laser power beaming can provide a continuous power supply to units operated within deep craters over the lunar

© 2025 The Author(s). Published by IOP Publishing Ltd

surface in the upcoming lunar missions, ensuring uninterrupted operations irrespective of their position relative to the Sun. Despite these advantages, challenges such as atmospheric attenuation, beam alignment, and safety concerns need to be addressed to fully realize the potential of LPT.

The efficiency of a LPT system depends on various components, including the laser source, the transmission medium and, most critically, the receiver. In particular, the receiver is based on multiple arrays of single photovoltaic (PV) cells connected in series and parallel, optimizing energy conversion while ensuring compliance with constraints such as the voltage required by the step-down converter. While PV panels developed for space applications [4] are highly effective at converting sunlight into electrical energy, they are not optimized for the monochromatic and coherent nature of laser light [5–7]. This mismatch leads to suboptimal conversion efficiency when traditional solar panels are used in laser power beaming systems. Therefore, developing PV panels specifically designed to efficiently convert laser light into electrical energy is essential for maximizing the effectiveness of LPT.

In this paper, we present two different PV panel designs based on a ring and tree arrangement of the cells. We perform a quantitative analysis of the optical-to-electrical conversion efficiency for both geometries, which takes into account variations in the parameters of the incident Gaussian laser beam along with thermal effects based on typical temperature coefficients, ultimately complying with the electrical parameters of a space-qualified laser power converter. We focus on lunar missions and the need to power machines at the bottom of deep lunar craters, where sunlight is intermittent and temperature conditions are extreme. To this regard, we develop a detailed thermal analysis accounting for the environment temperature of −246 °C, as measured by NASA's Lunar Reconnaissance Orbiter in deep craters near the poles [8], and the large temperature gradient induced by a high-power laser beam incident onto the PV panel.

Our analysis is developed around simulations of I–V and P–V curves of the PV system, with the objective of determining the system efficiency. Simulations predict a maximum efficiency of 37% for our ring-structured PV panel, approaching the 42.3% efficiency of the single PV cell operated below saturation at an intensity of 1 W cm^{-2} and at room temperature. We demonstrate that LPT technology is feasible and can achieve high performance comparable to state-of-the-art solar panels, even in a lunar environment, provided that the receiver is specifically designed to account for the monochromatic coherent light produced by lasers.

2. Basic principles for WPT

2.1. System architecture

The general architecture of a LPT system, shown in figure 1, includes a power conditioning and distribution unit (PCDU) for powering the laser, a high-power laser, a beam launch and collection optics, a PV panel, and a second PCDU for conditioning the power output from the panel [9–11]. Regarding the high-power laser, the most efficient, compact, and wavelength-compatible solutions have been identified in diode lasers at 976 or 940 nm, or Yb:fiber lasers at 1030 nm [12], with the first preferable in terms of reliability and compactness, and the second favored by the minimum-divergence beam when larger distances (>100 m) need to be covered [6]. As the application of interest here is a LPT system for lunar's crater with typical diameters ranging from 1 to 10 km, the analysis focuses on the case of Yb-fiber lasers. As for the receiver, an InGaAsP triple-junction laser power converter has been identified, based on efficiency and wavelength compatibility criteria [13, 14].

This study is conducted within the framework of the ARTEMIS program [15], with a specific focus on three key application cases: the European Charging Station for the Moon (ECSM), the *in-situ* resource utilization (ISRU), and the European Moon Rover System (EMRS). The ECSM has been designed to be integrated within the European Large Logistics Lander architecture, ensuring its transportation to the lunar surface, with the aim of providing a continuous and reliable power supply at a strategically significant lunar location to support both ESA and international partner assets. A reference use case for ECSM is the Astronaut Science Enabler (AstroSci), which necessitates a continuous power supply of ∼7.7 kW during the lunar day. The ISRU study focuses on the conceptual design of a pilot plant dedicated to oxygen extraction from lunar regolith. This facility is regarded as a critical component of the mission scenario; when operated in production mode, the ISRU system has a power demand of ∼7.8 kW. Finally, the EMRS has been conceptualized to address the requirement for a mobility solution during lunar missions, with an estimated power consumption of approximately 500 W. According to these application cases, throughout this analysis, it is assumed that the power required by the end-user device is within the range of 0.5–8 kW. In addition, considering the specifications outlined by European Cooperation for Space Standardization [16], the PCDU is constructed upon a 100 V bus. The bus voltage imposes a constraint on the minimum number of cells in series that each string must have because the voltage drop across the series must be higher than the bus voltage. A high-efficiency step-down converter transforms the voltage from the panel to the bus. Our design is based on a division of the PV panel into sections, each of which has its own step-down converter.

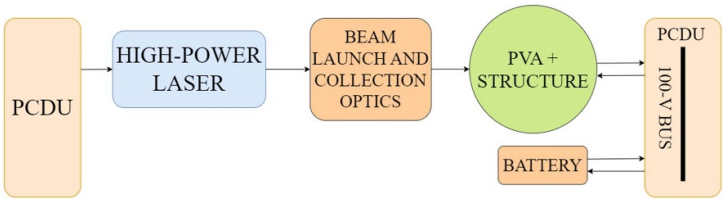

Figure 1. LPT system architecture.

2.2. Gaussian beams

Laser sources such as the multi-kW class Yb-fiber lasers considered here, are characterized by a non-uniform intensity distribution of the output beam in the far field, which is well approximated by the space-dependent Gaussian intensity [17, 18]

$$I(r,z) = I_0 \left(\frac{w_0}{w(z)}\right)^2 \exp\left(-\frac{2r^2}{w(z)^2}\right) \tag{1}$$

where $I_0 = 2P/(\pi w_0^2)$ represents the peak intensity, w_0 is the beam radius at the waist, $w(z) = w_0(1 + (z/z_R)^2)^{1/2}$ is the beam radius at a distance z from the waist, P is the average power of the beam, r is the radial coordinate and z_R is the Rayleigh range. Space-dependent intensity makes the design much more complicated compared to the case of uniform solar distribution, because the single cells over the surface of the PV panel are operated at different incident intensities, hence different operating points along the I–V curve [19]. This requires optimization of the panel geometry, specifically the arrangement of series and parallel connections between cells, to avoid bottle-necking effects on the photocurrents. In addition, temperature variations between different parts of the panel must be taken into proper account for an accurate modeling of system performance. The radial beam intensity distribution, as expressed in 1, can be more conveniently expressed as a function of the beam spot size w and the optical power P, as it follows:

$$I(r) = \frac{2P}{\pi w^2} \exp\left(-\frac{2r^2}{w^2}\right). \tag{2}$$

This formulation simplifies the evaluation of panel performance following the variations in peak intensity I_0 and beam spot size w. Assuming a constant beam power P, (2) enables an effective analysis of panel performance by systematically varying w and $I_0 = 2P/(\pi w^2)$.

3. PV array

The study of the receiver design is generally based on the selection of its geometry and array configuration. The geometry is the arrangement of cells, strings and sections on the surface of the panel. The array configuration is the interconnection scheme, i.e. how the cells and strings are connected. A number of configurations have been proposed as a means of mitigating the effects of non-uniform intensity profiles or partial shading conditions [20]. These include the standard series-parallel (SP) configuration, the total-cross-tied (TCT), bridge-linked (BL), and honeycomb (HC) configurations, which have been the subject of previous investigation [5, 6, 21]. In terms of simplicity of implementation and low cost, the SP and TCT configurations turn out to be the best solutions.

In this article, we mainly consider the geometric aspects and present two radial geometries: the Ring-Shaped design and the Tree-Shaped design. In the context of these geometries, the SP configuration is identified as the optimal solution for describing the interconnection scheme among the cells. The standard SP configuration, even if it is generally unsuitable for accommodating the Gaussian intensity distribution of the laser beam, is identified as the optimal solution for describing the interconnection scheme among the cells, thanks to a very precise calibration of the geometry. Therefore, a section is constituted by sets of parallel-connected strings, with the strings themselves comprising sets of series-connected cells, as illustrated in figure 2. We explored a range of alternative configurations, including TCT, HC, and BL interconnections [5, 6]. However, given the comparatively negligible efficiency gain of these configurations with respect to the standard SP configuration, and considering the increased complexity associated with their practical implementation, we opted for a geometrical approach while maintaining the standard SP configuration. This choice ensures a balance between performance optimization and feasibility, prioritizing a design that is both efficient and straightforward to implement. Furthermore, regarding the geometry, we required cylindrical

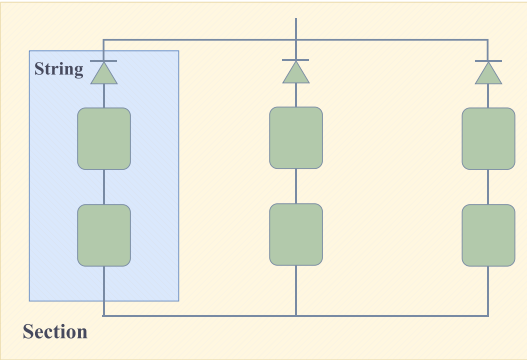

Figure 2. The structure of a PV panel made of strings and sections with the standard SP configuration.

symmetry to match the Gaussian spatial profile of the incident beam. This necessitated a circular panel design, ensuring optimal power collection across the illuminated area. Additionally, the strings could not be too long along the radial direction, as the current of the entire string is limited by the most peripheral cell. A long radial string would lead to higher current mismatches due to the beam intensity decreasing towards the edges, reducing the overall efficiency. Therefore, the panel design was optimized to minimize such losses while maintaining a practical interconnection layout.

A non-uniform intensity distribution, causes thermal excursions within the panel, impacting the electrical parameters of the cells. To the best of our knowledge, a quantitative analysis of this configuration including thermal effects has not yet been reported.

3.1. Theoretical background

The PV cell is a device that converts light energy into electrical energy. Its operation is based on the PV effect, where a potential difference is created between two different materials when photons illuminate the junction. When the junction absorbs photons, this energy is transferred to the electronic band structure of the material, resulting in the generation of charge carriers that separate at the junction. Any power that is not converted into electricity either remains in the junction, increasing its temperature, or is dissipated through thermal radiation into the surrounding environment. The parameter that provides a benchmark of the cell performance is the optical-to-electrical efficiency η, defined as the ratio of output electrical power to input optical power

$$\eta = \frac{P_{\text{out}}^{\text{el}}}{P_{\text{in}}^{\text{opt}}}. \tag{3}$$

The PV cell can be modeled using an equivalent electrical circuit [22] in which it acts as a current generator in parallel with a shunt diode, as shown in figure 3. The series resistance represents the internal resistance of the cell, while the shunt resistance accounts for losses through the junction. In an ideal cell, the series resistance is negligible, and the shunt resistance is infinite, indicating no losses. Among other parameters of the cell are the open-circuit voltage (V_{oc}) and the short-circuit current (I_{sc}). The open-circuit voltage is the voltage across the terminals of the cell when no load is applied. In addition, as shown in figure 3, every cell has a shunt diode connected in parallel as a protective circuit. Let I and V be the load current and voltage respectively. The open-circuit voltage V_{oc} can be expressed as

$$V_{\text{oc}} = V + IR_{\text{s}} \tag{4}$$

The current through the diode I_{d} is given by

$$I_{\text{d}} = I_0 \left[\exp\left(\frac{qV_{\text{oc}}}{AkT}\right) - 1\right] \tag{5}$$

where A is the diode ideality factor, R_{s} is the series resistance, k the Boltzmann constant, T is the absolute temperature and I_0 the saturation current. Therefore, the load current can be expressed as

$$I = I_{\text{s}} - I_0 \left[\exp\left(\frac{qV_{\text{oc}}}{AkT}\right) - 1\right] - \frac{V_{\text{oc}}}{R_{\text{sh}}} \tag{6}$$

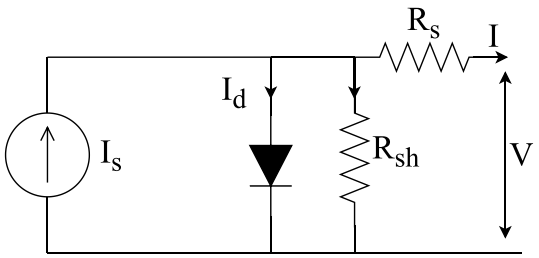

Figure 3. Equivalent electrical circuit for the PV cell. R_{sh}: shunt resistance; R_s: series resistance; I_d: diode current; I_s: PV cell photocurrent.

Table 1. Electrical parameters of PV cell.

Electrical parameter	Value
Efficiency (1 W cm^{-2}, 25°C)	42.3%
Short-circuit current density, J_{sc}	237.5 mA cm^{-2}
Open-circuit voltage, V_{oc}	2.174 V
Maximum power point voltage, V_{MPP}	1.883 V
Maximum power point current density, J_{MPP}	224.2 mA cm^{-2}
Temperature coefficient α J_{sc}	5.3 μA °C^{-1}
Temperature coefficient β V_{oc}	5.9 mV °C^{-1}
I_{shunt}^{diode}	0.1 mA

where I_s is the photocurrent [23]. Equation (6) defines the single-diode model illustrated in figure 3. Several authors have proposed more advanced models that offer greater accuracy and address different objectives. For example, in [24, 25], an additional diode is introduced to account for carrier recombination effects. Similarly, a three-diode model is presented in [26] to incorporate phenomena not considered in previous models. Nonetheless, equation (6) provides a balanced trade-off between simplicity and accuracy [27] and has been widely adopted in previous studies for the simulation of PV devices with power converters [28–30].

The calculation of electrical parameters at the section level includes the evaluation of the section thermal voltage and the reverse saturation current, and it is performed as follows. The maximum power point current of the section is calculated using:

$$I_{mp}^{sec} = \left(J_{mp}^{cell} S - I_{shunt}^{diode}\right) N_{string}^{sec} \tag{7}$$

where S is the effective area of the cell. The short-circuit current of the section is once again the product of the short-circuit of the cell by the number of strings in the section,

$$I_{sc}^{sec} = \left(J_{sc}^{cell} S - I_{shunt}^{diode}\right) N_{string}^{sec} \tag{8}$$

where J is the current density. The thermal voltage of the section is:

$$V_t^{sec} = V_{mp}^{cell} \frac{I_{sc}^{sec} - I_{mp}^{sec}}{I_{mp}^{sec}}. \tag{9}$$

The reverse saturation current is:

$$I_{sat} = \frac{I_{sc}^{sec}}{\exp\left(V_{oc}/V_t^{sec}\right) - 1}. \tag{10}$$

In this paper we assume that each cell has a parallel-connected bypass diode and a blocking diode is connected in series with each of the series strings as shown in figure 2. The electrical parameters of the cells are summarized in table 1. The cell is based on vertically-stacked InGaAsP triple-junctions providing maximum conversion efficiency of 42.3% at a power density of 1 W cm^{-2} under 1064 nm laser irradiation at room temperature with an open-circuit voltage of 2.16 V. Higher conversion efficiencies such as 45% have been even demonstrated in Si cells with complex pyramid-textured surface [31], however, the InGaAsP triple-junction cell adopted here can be grown by conventional metal–organic chemical vapor deposition while still providing improved conversion efficiencies at 1030 nm [13].

3.2. Thermal effects

In our analysis, we assume that the receiver is placed in a permanently shaded area of the lunar surface. Therefore, we consider the typical temperatures in this environment as well as the fact that the only source of incident light on the panel is provided by the laser. We do not consider either sunlight or the portion of light reflected from the lunar surface (albedo). The temperature of a section of the panel is calculated using Newton's method, taking into account the balance resulting from the output power of the incident laser beam P_{laser}, the electrical power delivered by the panel, $P_{\text{el}}^{\text{out}}$, and the net power radiated into space, $\Delta P_{\text{rad}} = \varepsilon\sigma(T - T_0)^4$

$$P_{\text{laser}} = P_{\text{el}}^{\text{out}} + \Delta P_{\text{rad}}. \tag{11}$$

The Stefan–Boltzmann law is employed to compute $\varepsilon\sigma(T - T_0)^4$, taking into account the incident power generated by the lunar environment, which is assumed to be at $T_0 = 27$ K, the emissivity of the layer, ε, and the Stefan–Boltzmann constant, σ [9–11].

The thermal spatial profile of a two-dimensional PV panel composed of InGaAsP cells is modeled using COMSOL Multiphysics [32], employing the finite element method to achieve an accurate discretization of the PV array surface. The panel is subjected to a Gaussian illumination profile, and its thermal response is analyzed in an environment with an extremely low ambient temperature. The balance of heat is determined by the interplay between the absorbed radiation, the mechanisms of heat dissipation, primarily radiative losses, given the negligible role of convective heat transfer under these conditions and the electrical conversion. The model incorporates the relevant thermophysical properties of InGaAsP, including its thermal conductivity, specific heat capacity, and density [13, 14]. The absorbed power distribution is defined based on the material's properties, accounting for the penetration depth of the incident radiation. The dissipation of heat is principally determined by radiative emission, which is modeled according to the Stefan–Boltzmann law. The computational approach employs a structured quadrilateral mesh, with refinement in regions exhibiting steep thermal gradients. The simulation is performed in steady-state conditions, to determine the equilibrium temperature distribution.

Figure 4 shows the temperature variation as a function of peak intensity for different fill factors (FFs). The FF represents the percentage of surface area occupied by the cells on the panel surface. At a given peak intensity of the incident laser, the temperature of the panel decreases as the FF increases, because of the larger electrical power extracted form the panel. Figure 5 illustrates the thermal map of the panel exposed to a Gaussian intensity distribution with peak intensity of 1600 W m^{-2}. The temperature ranges from a minimum of 27 K, corresponding to the environment temperature at the bottom of a deep crater, to a maximum of 395 K; this large temperature gradient attests the needs for a detailed thermal modeling to get accurate predictions on the global efficiency of the panel. Figure 5 also displays the Gaussian intensity and the temperature profile along a vertical section of the panel; the mismatch between the two profiles is apparent.

The temperature induces variations in the energy bandgap according to the Varshni relation [33], expressed by

$$E_{\text{g}}(T) = E_{\text{g}}(0) - \frac{\gamma T^2}{\delta + T} \tag{12}$$

where $E_{\text{g}}(T)$ and $E_{\text{g}}(0)$ are respectively the energy bandgap at temperature T and 0 K, γ and δ are two empirical parameters which are typical of the material. A temperature variation of 300 °C induces a variation in the energy bandgap of the InGaAsP triple junction considered in this study corresponding to a wavelentgth shift within the range of 1000–1100 nm [13]. In this wavelength range, the external quantum efficiency is substantially flat, hence the temperature-induced bandgap shift exerts minimal influence on the spectral properties of the PV cell. From a macroscopic perspective, temperature influences the electrical parameters of a PV cell. Specifically, temperature variations impact both the short-circuit current and the open-circuit voltage, with these effects governed by the corresponding temperature coefficients, α and β, according to the relations

$$I_{\text{sc}} = I_0^{\text{sc}} + \alpha\Delta T \tag{13}$$

$$V_{\text{oc}} = V_0^{\text{oc}} - \beta\Delta T \tag{14}$$

where I_0^{sc} and V_0^{oc} represents the short-circuit current and open-circuit voltage at temperature T_0. Note the opposite signs of the induced current and voltage variations. As a result of the temperature gradient, the electrical power generated by the cell changes to

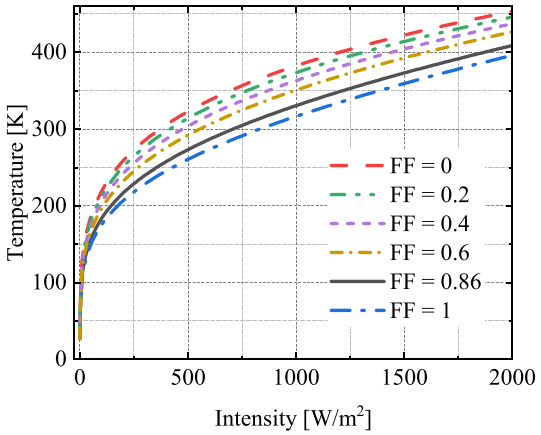

Figure 4. Temperature as a function of incident intensity for a panel section composed of three 32-cells strings for six different fill factors.

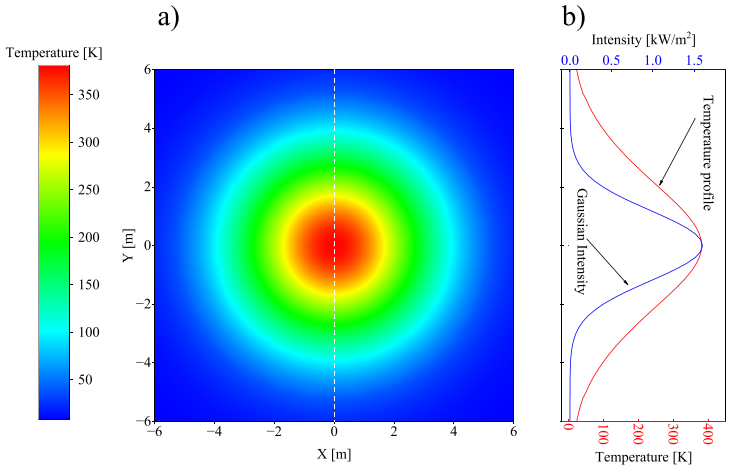

Figure 5. (a) Two-dimensional thermal map of the panel exposed to a Gaussian beam with 1600 W m^{-2} peak intensity. (b) Comparison between the temperature profile and the Gaussian intensity distribution across a vertical section of the panel. The thermal spatial profile of the two-dimensional InGaAsP PV panel is modeled by finite element analysis.

$$P = VI = (I_0^{sc} + \alpha\Delta T)(V_0^{oc} - \beta\Delta T) \tag{15}$$

$$= P_0 - [(\beta I_0^{sc} - \alpha V_0^{oc})\Delta T]. \tag{16}$$

Figures 6 and 7 show the current–voltage and power–voltage curves associated with a section of the panel illuminated by uniform irradiance with the temperature set independently. It can be noted that the maximum extracted power is inversely proportional to the temperature, as a result of the large mismatch between the open-circuit voltage and short-circuit current temperature coefficients, with the former being much larger than the ladder. Figure 8 represents a panel section under condition of non-uniform irradiance, specifically composed of three strings with three different incident intensities and, accordingly, three different operating temperatures. Note the appearance of local modulations in the I–V Curve due to the non-uniformity of the illumination. The phenomenon is characterized by the presence of three distinct levels of currents and voltages across the three strings. The three levels of voltage are determined by the three distinct working temperatures of the strings. Regarding the currents, the higher the intensity, the greater the current produced by each string. Consequently, each string has its own I–V curve, and the current of the entire section is the sum of the three currents, with the voltage remaining consistent across the three strings due to their parallel connection. The P–V curve shows an increasing trend until the maximum power point voltage and then a decreasing modulated trend. The modulations correspond to the three levels of currents produced by each string. The absence of modulations in the increasing region of the P–V curve is due to the corresponding constant behavior of the current in the I–V graph.

Note that the optical-to-electric efficiencies reported throughout this study are calculated at the maximum power point of the PV strings. The rationale behind this definition is as follows: first, the I–V

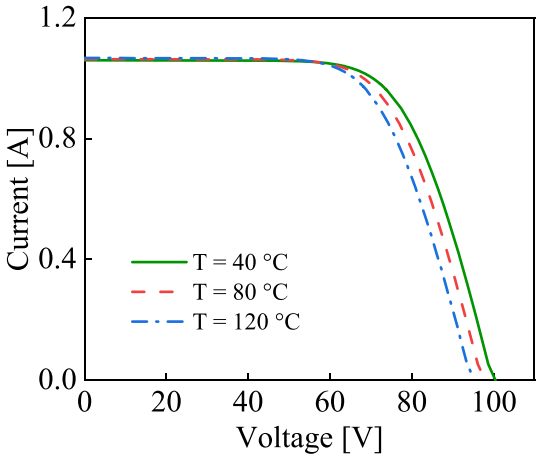

Figure 6. *I–V* Curves for a section composed of three 32-cells strings at three different temperatures, peak intensity of $I_0 = 1.6\,\mathrm{kW\,m^{-2}}$, and beam radius w of 2.82 m.

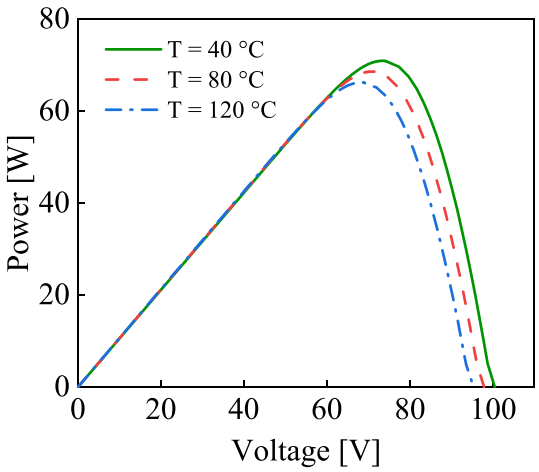

Figure 7. P-V Curves for a section composed of three 32-cells strings at three different temperatures, peak intensity of $I_0 = 1.6\,\mathrm{kW\,m^{-2}}$, and beam radius w of 2.82 m.

curve for each section of the array is evaluated; then, the maximum power point voltage and current are extracted from each curve, and the corresponding electrical power extracted at each section is calculated; finally, the summation of power contributions from all sections yields the total power extracted from the PV array. The optical-to-electrical conversion efficiency is thus defined as the ratio between the power extracted from the PV array, according to the rationale outlined, to the incident optical power. For simplicity, the term efficiency will be used in the remainder of this paper.

3.3. Ring-Shaped geometry

The first design proposed for the PV panel is based on the intuitive concept that the geometry and arrangement of cells within the panel must resemble the cylindrical symmetry of the laser beam about the propagation axis, therefore it should have a circular shape. At this stage, considerations arise regarding thermal excursion along the radial direction of the panel, as well as the Gaussian distribution of intensity, which intuitively leads to a decreasing power generation as one moves away from the center of the panel. To minimize these effects, the receiving surface has been divided into rings of a thickness such that thermal excursion is minimized. Since the architecture utilizes a 100 V bus associated with a step-down converter, the *I–V* curve of each section must have the voltage corresponding to the maximum power point above the bus voltage. Therefore, we have a constraint on the length of a string within each section. However, as we move away from the center of the panel, the temperature decreases, and the open-circuit voltage exhibits an increasing trend as the temperature decreases (and vice versa). The lower limit on the thickness of a ring is determined by the smallest cell dimensions. Specifically, the minimum size of the cell is the minimum dimension of the shorter side. The size is determined by the sum of the shorter side and the minimum

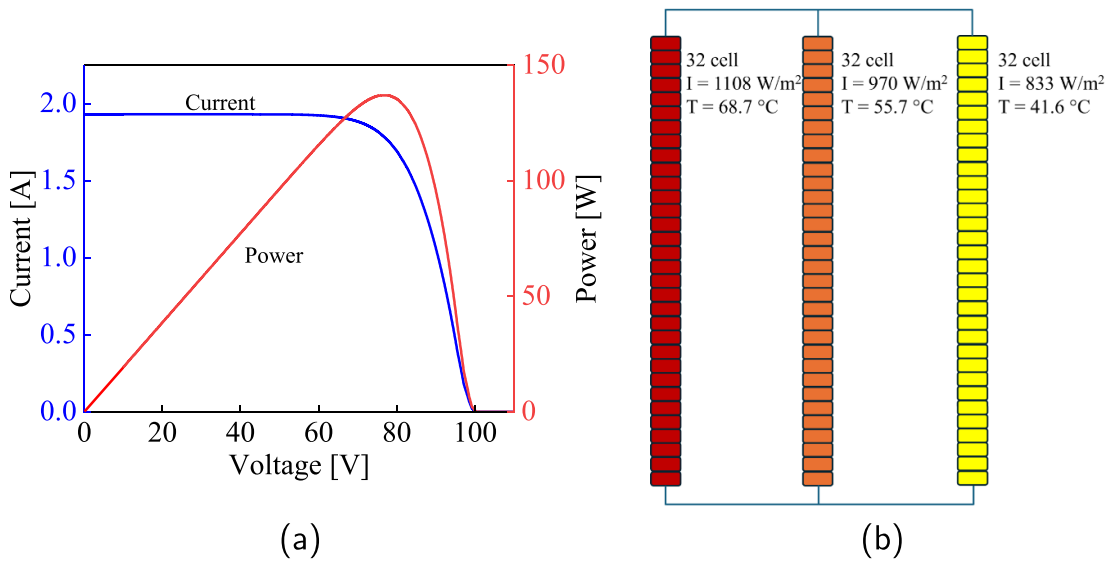

Figure 8. The *I–V* and *P–V* curves resulting from the parallel of three 32-cells strings operated at three different incident intensities and corresponding temperatures. The intensities and temperatures are 833 W m^{-2}, 970 W m^{-2}, 1108 W m^{-2} and 41.6 °C, 55.7 °C, 68.7 °C, respectively. (b) Scheme of the different intensity and temperature levels of the three strings.

distance between cells, which is required to give room for wiring while avoiding, at the same time, discharges between cells at different potentials. Electrical discharges between points at different potentials occur when the electric field exceeds the dielectric strength of the material. In a space environment, to avoid ESD phenomena the good practice imposes at least for 1 mm gap between adjacent non-directly connected cells with differential voltage up to 30 V [16]. In the worst-case scenario, the first and last cell of a string are placed in adjacent positions, and the corresponding potential difference is of approximately 100 V. Therefore, a distance of 4 mm between cells is mandatory to avoid for electrical discharge; as a consequence, an overall 4.4 cm extent must be accounted for each cell, as shown in figure 9. The surface area of the PV array is determined by the summation of the total area occupied by each individual cell, taking into account a FF of 0.86; the corresponding surface intensity is obtained as the ratio of the incident optical power to the surface area of the PV panel. The criteria used for proper sizing of the rings are based on the following considerations: first, each section placed within a ring must have a minimum length that allows for the voltage of the maximum power point being above the bus voltage; second, the design cannot be based on the assumption that all sections must generate same electrical power, as in this case, peripheral sections would have prohibitively extended surfaces; third, the design cannot be based on the assumption that each section shall be of the same surface, as in this case the radial size of a section shall decrease according to a $1/r^2$ law, which is not feasible since the minimum radial extent is limited by the minimum dimension of a cell. The most reasonable compromise between these considerations is represented by Ring-Shaped sections with constant thickness. The ring-like sections may contain more than one string, or alternatively, a single folded string. In this case, the cells in a single-folded string are located at different distances from the center. The current of the string is the current produced by the cell located at larger distance in the ring of radii R_1 and R_2. Therefore, the current of each string is determined by the current from the cell located at the larger radius of the ring. At the same time, the temperature of the section is approximated to the average temperature observed at the center of a section, with the highest temperature at a distance R_1 from the center, and the lowest at a distance R_2. Figure 10 shows the interconnection scheme of the Ring-Shaped design. Figure 11 illustrates the trend of the efficiency as a function of the peak intensity of the incident beam. It's worth noting that the efficiency decreases as the peak intensity increases. This is mainly ascribed to the large gradient of the Gaussian intensity distribution which in turn induces a large temperature gradient across the panel ultimately reducing the overall efficiency. For reference, the efficiency of the single-cell power converter at 1 W cm^{-2} and 25 °C is also shown. Figure 12 shows the trend of electrical output power as a function of optical input power at different peak intensities. The trend is steeper at lower peak intensities because the Gaussian profile gets smoother, approaching a more uniform intensity distribution, resulting in improved efficiency. Figure 13 shows the extent of the panel surface as a function of the peak intensity. The extension of the panel is mainly related by the beam spot size. Keeping constant the input optical power, the minimum surface is given by the most intense beam. Furthermore, we also imposed a limit on the temperature at the center of the panel around 150 °C. It follows that the peak intensity has a further upper limit given by the temperature

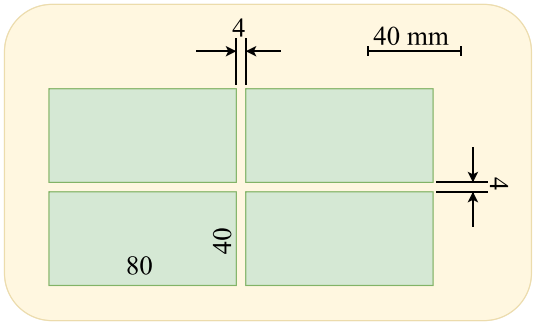

Figure 9. Typical arrangement of PV cells over solar panels; the dimensions of a single cell are 40 mm × 80 mm. A clearance of 2 mm is left along each side of a cell to maintain a 4 mm gap between adjacent cells and therefore to prevent electrical discharge.

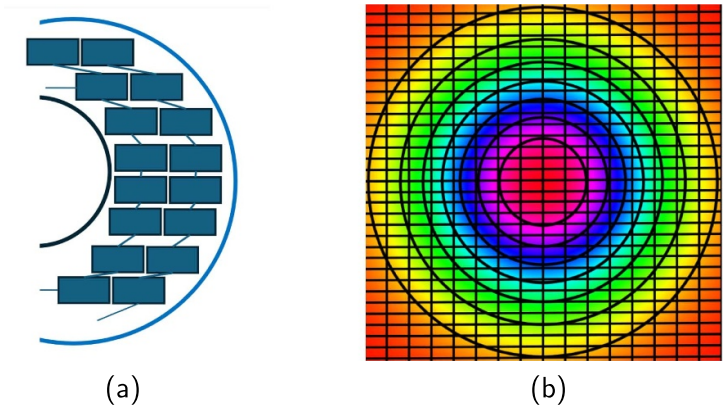

Figure 10. Ring-Shaped design. (a) 8-cell strings in Ring-Shaped design interconnection scheme. (b) Optical field intensity across the cells.

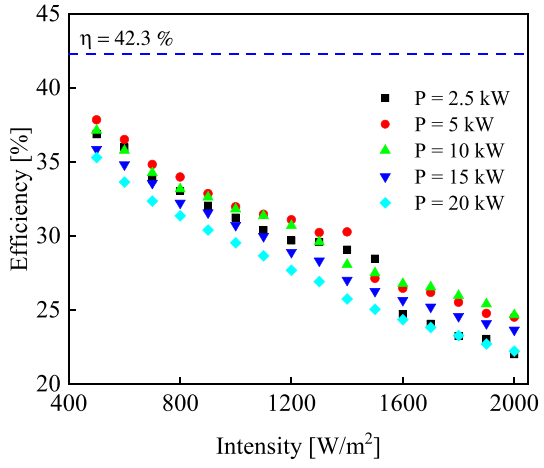

Figure 11. Efficiency versus peak intensity for the Ring-Shaped design at varying incident optical powers. The dashed line represents the efficiency of a single-cell laser power converter (1 W cm^{-2}, 25 °C).

corresponding to this temperature. A little bit more in detail, the surface of panel is $\propto \pi w^2$. It follows that the surface trend is $\propto P/I$ where P is the power and I the peak intensity. The intensity distribution is defined for $0 < r < +\infty$. Consequently, in order to collect the entire beam, it is necessary to create an infinite-extended panel. Therefore, a threshold for the radius must be set, beyond which the sections will convert a negligible power with respect to the fully-collected beam. The threshold radius has been established at $r \simeq 1.5w$, as the converted power of a section beyond this distance is less than 1% of the total power.

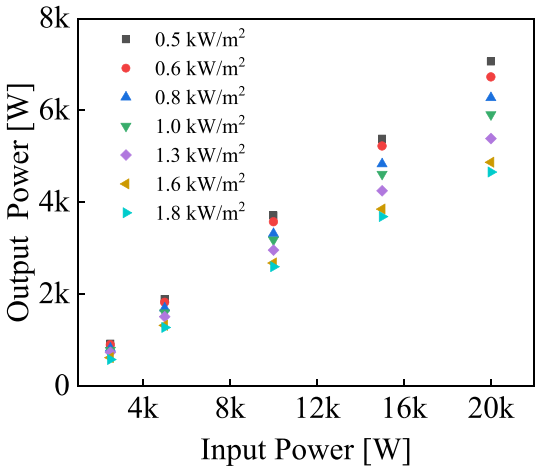

Figure 12. The electrical output power as a function of optical input power for the Ring-Shaped design at different peak intensities of the beam.

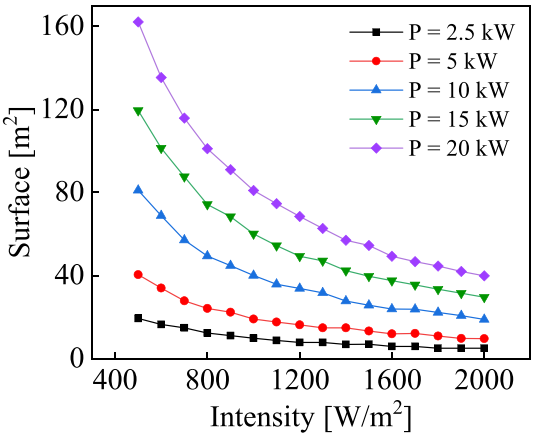

Figure 13. Panel surface extent as a function of peak intensity for the Ring-Shaped design at different input optical powers.

3.4. Tree-Shaped geometry

The second design proposed for the PV panel is based on a Tree-Shaped geometry, where the circular panel is divided into circular sectors, with each sector comprising four sections connected in series, as shown in figure 14. The Tree-Shaped design allows for placing several strings in parallel within a section which compensates for the reduced Gaussian beam intensity at a large distance from the center. Each sector is made of four sections connected in series, meaning that the current through the entire sector is determined by the lowest current among the four sections. Each section is characterized by its own I–V curve. The current through a string in a section is determined by the cell located in the most peripheral position. At this point, each section will have its own voltage and current of maximum power point V_{mp} and I_{mp}, respectively. The current through the entire circular sector is therefore the minimum among the four I_{mp}, and the voltage will be the sum of the four maximum power point voltages. One main advantage of the Tree-Shaped structure lies in the scalability of the system. Indeed, it is sufficient to optimize the design of a single circular sector and then scale it up based on the number of circular sectors needed to fill the panel.

Similar to the case of a Ring-Shaped design, the Tree-Shaped design is characterized by a decreasing trend of efficiency as a function of peak intensity of the Gaussian profile, as shown in figure 15. Figure 16 shows the trend of the electrical output power vs the optical input power for different peak intensities. The considerations made above for the Ring-Shaped design can be extended also in this case. Again, as we can observe in figure 17, the surface of the panel strongly depends on the peak intensity of the beam and it follows a decreasing trend as the intensity increases. For this type of design the surface has been computed in a different way with respect to the previous case. The lengths of the strings has been used to determine the extension of the single circular sector. The circular sector is then used to evaluate the entire surface of the panel. Since the lengths of the strings are optimized to obtain the maximum power, the four series-connected

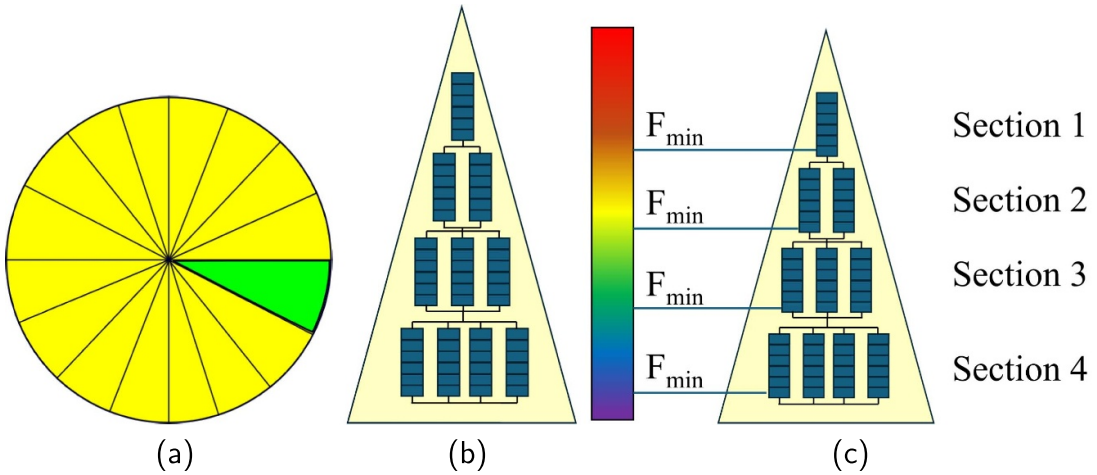

Figure 14. Tree-Shaped design. (a) Circular panel. (b) Each circular sector is composed of a certain number of sections connected in series. (c) Circular sector with sections of varying lengths. The gradient bar indicates the intensity at the cell locations.

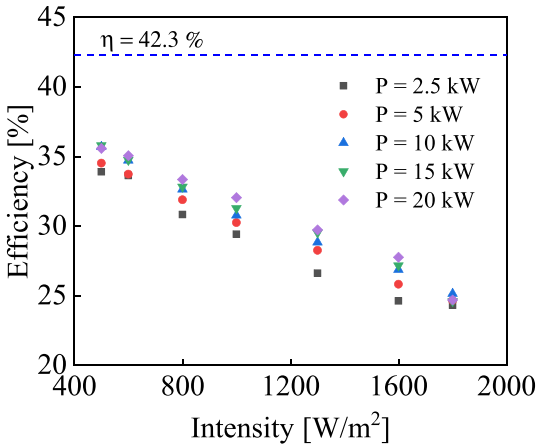

Figure 15. Electrical-to-optical efficiency vs peak intensities for different input optical powers in the Tree-Shaped design. The dashed line represents the efficiency of a single-cell laser power converter (1 W cm^{-2}, 25 °C).

sections have to produce comparable currents. If the most peripheral cells in the last section are too far from the center, the current of the last section can negatively influence the current of the entire circular sector, thus the power of the entire panel. It follows that the optimal radius of the panel is $r \simeq 0.9w$ and the reason of a lower efficiency with respect to the previous design is also due to a smaller effective area which collects the beam.

4. Discussion

Simulations performed on the electrical-to-optical efficiency show that smoother Gaussian distributions (i.e. lower peak intensities) allows for improved conversion into electrical power. Alternatively, assuming a laser beam of fixed optical power, the overall efficiency decreases with the peak intensity by several percentage points because high intensities correspond to high temperatures and because increasing the peak intensity increases the slope of the Gaussian.

It is particularly evident that the temperature exerts a substantial influence on the performance of a PV array, predominantly affecting pivotal electrical parameters such as open-circuit voltage, short-circuit current, and maximum power output. As the temperature rises, the bandgap energy of the semiconductor decreases, leading to a reduction in the open-circuit voltage. This decline in voltage is the predominant factor contributing to the overall decrease in power output at higher temperatures. Conversely, the short-circuit current exhibits a slight increase with temperature due to enhanced carrier generation rates. However, this variation is relatively insignificant, and thus incapable of compensating for the concurrent voltage drop. The maximum power output $V_{mp}I_{mp}$ is thus negatively affected by temperature, since it is dependent on both the

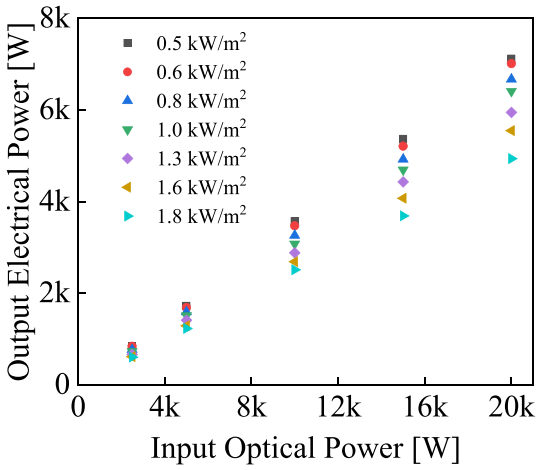

Figure 16. Output electrical power vs input optical power for different peak intensities in the Tree-Shaped design.

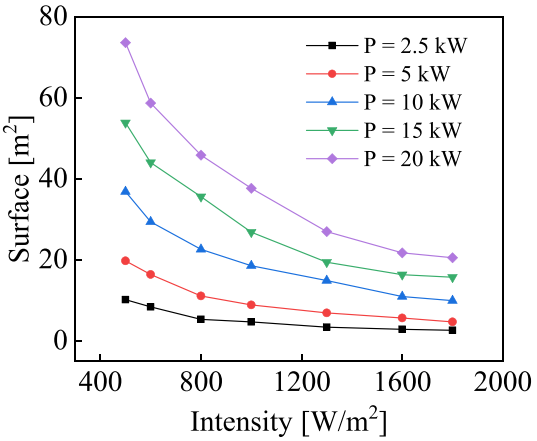

Figure 17. Surface vs peak intensity for different input optical powers for the Tree-Shaped design.

voltage and current at the maximum power point. Furthermore, the ratio $(V_{mp}I_{mp})/(V_{oc}I_{sc})$ is adversely influenced by temperature due to the combined effects of voltage reduction and increased series resistance. This results in a more pronounced curvature in the current–voltage characteristic, which ultimately reduces the efficiency of the PV array. In summary, high temperatures have a detrimental effect on the efficiency of a PV module. Given these effects, thermal management plays a crucial role in mitigating performance degradation. The implementation of effective strategies, such as incorporating passive heat dissipation mechanisms, can substantially mitigate thermal losses and enhance the overall efficiency of the system.

Theoretically, the best optical-to-electrical conversion efficiency is achieved at peak intensities below 500 W m^{-2} (as typically used in testing phases). In the context of a space program the definition of the mass budget for a PV array is fundamental. The panel size as a function of peak intensity is characterized by a decreasing trend, for both the Ring-Shaped and Tree-Shaped design.

The Ring-Shaped design represents the most efficient proposal, achieving an efficiency of 37% at 500 W m^{-2}. The Tree-Shaped design exhibits slightly lower efficiency of 35.6% in similar conditions. In both cases, increasing the peak intensity to 1800 W m^{-2} results in a reduction of efficiency of over 10%. However, in contrast to the Ring-Shaped design, the Tree-Shaped design exhibits a more compact surface area, as illustrated in figures 13 and 17. A future iteration of the research could be based on a hybrid configuration, combining the Tree-Shaped design for $r < 0.9w$ and the Ring-Shaped design for $0.9w < r < 1.5w$. This would effectively combine the scalability of the second design with the efficiency of the first.

Finally, it is worth considering how the LPT solutions proposed here meet the application needs of ECSM, ISRU, and EMRS, mentioned before. To this regard, the ∼8 kW power requirement of ECSM and ISRU can be approached by using a 20 kW laser source illuminating a PV panel with an extension of ∼160 m^2 (diameter of ∼7 m^2) operated at a peak intensity of 500 W m^{-2}. On the other side, the 500 W requirement of EMRS is reached with a 2 kW laser source and a PV panel with an extension ∼10 m^2

(diameter of ∼3.6 m^2) operated at a peak intensity of 500 W m^{-2}; basing on this, the total mass of the PV array results to be around 10% of the 300 kg EMRS lunar rover, making this configuration very feasible.

5. Conclusion

This paper presents a quantitative analysis aimed at exploring the potential of a wireless energy transmission system based on a laser transmitter and a PV panel receiver. Numerical simulations are used to assess both power and efficiency within the extremely challenging environment of a deep lunar crater, assuming a base temperature as low as 27 K. Two possible receiver geometries, called the Ring- and Tree-Shaped geometry, are presented, both based on the use of an SP configuration. As a main result of the simulations, peak efficiencies of up to 37% have been calculated, positioning this technology competitively with space-qualified solar cells currently accessible in the market, despite still being in the developmental phase for space qualification. It is demonstrated that the non-uniformity of the intensity and temperature profiles, typical of a Gaussian laser beam, represents a main technological issue which impacts the electrical parameters and therefore needs to be addressed by introducing a specifically tailored design and configuration of cells within the PV panel. It should be noted that the very low temperature characterizing the lunar environment helps improving the performance of a PV array. Significant improvements of optical-to-electrical efficiency could be obtained by optimizing the FF of the panel, perhaps by altering the shape of the cell, and enhancing the efficiency of an individual cell. Further analysis on the design of the PV panel will take into account the average duration of a lunar mission and focus on investigating the impact of degradation factors such as radiation, micrometeorites, and lunar dust, on the electrical parameters, thus allowing an estimation of end-of-life efficiency.

In conclusion, this study investigates a LPT system as a potential solution to support these high-power lunar applications. The utilization of such a system would facilitate wireless energy transfer, thereby enabling continuous and efficient operation in the challenging lunar environment.

Data availability statement

The data cannot be made publicly available upon publication because the cost of preparing, depositing and hosting the data would be prohibitive within the terms of this research project. The data that support the findings of this study are available upon reasonable request from the authors.

ORCID iDs

Giovanni Cichelli https://orcid.org/0009-0003-8999-4629
Paolo Laporta https://orcid.org/0000-0003-2673-6983
Nicola Coluccelli https://orcid.org/0000-0001-9397-619X

References

[1] Yang T and Jin K 2020 A method of simultaneous transmission of power and information based on laser power transfer system *2020 IEEE Applied Power Electronics Conf. and Exposition (APEC)* (IEEE) pp 3159–62
[2] Mukherjee J, Wulfken W, Hartje H, Steinsiek F, Perren M and Sweeney S J 2013 Demonstration of eye-safe (1550 nm) terrestrial laser power beaming at 30 m and subsequent conversion into electrical power using dedicated photovoltaics *2013 IEEE 39th Photovoltaic Specialists Conf. (PVSC)* (IEEE) pp 1074–6
[3] Smith M, Tillotson B, Oliver J, Tarasenko N, Schoelzel T and Brandhorst H 2012 Development of a laser power beaming experiment *2012 38th IEEE Photovoltaic Specialists Conf.* (IEEE) pp 002825–30
[4] Summerer L and Purcell O 2009 *Europeans Space Agency (ESA)-Advanced Concepts Team*
[5] Zhou W and Jin K 2016 *IEEE Trans. Power Electron.* **32** 3662–72
[6] Jin K and Zhou W 2019 *IEEE Trans. Power Electron.* **34** 3842–59
[7] Zheng Y Zhang G Huan Z Zhang Y Yuan G Li Q Ding GLv Z Ni W Shao Y 2024 Space solar power and wireless transmission
[8] Farrell W M, Hurley D M, Poston M J, Hayne P O, Szalay J R and McLain J L 2019 *Geophys. Res. Lett.* **46** 8680–8
[9] Chen Q, Liu Z, Zhang X and Zhu L 2020 *Spacecraft Power System Technologies* (Springer)
[10] Hyder A K, Sabripour S, Flood D, Halpert G, Wiley R and Hyder A 2000 *Spacecraft Power Technologies* vol 1 (Imperial College Press London)
[11] Patel M R 2004 *Spacecraft Power Systems* (CRC press)
[12] Duncan K J 2016 Laser based power transmission: component selection and laser hazard analysis *2016 IEEE PELS Workshop on Emerging Technologies: Wireless Power Transfer (WoW)* pp 100–3
[13] Yin J, Sun Y, Yu S, Zhao Y, Li R and Dong J 2020 *J. Semiconduct.* **41** 062303
[14] Woo R L, Hong W D, Mesropian S, Leite M S, Atwater H A and Law D C 2011 First demonstration of monolithic InP-based InAlAs/InGaAsP/InGaAs triple junction solar cells *2011 37th IEEE Photovoltaic Specialists Conf.* pp 000295–8
[15] Nasa (available at: https://www.nasa.gov/mission/artemis-iii/)
[16] ESA 2008 Ecss-e-st-20c space engineering electrical and electronic copyright 2008 © by the european space agency for the members of Ecss

[17] Hodgson N and Weber H 2013 *Optical Resonators: Fundamentals, Advanced Concepts and Applications* (Springer)
[18] Siegman A E 1986 *Lasers* (University Science Books)
[19] He T, Zheng G, Liu X, Wu Q, Wang M, Yang C and Lv Z 2022 Analysis and experiment of laser wireless power transmission based on photovoltaic panel *Photonics* **9** 684
[20] Bayrak F, Erturk G and Oztop H F 2017 *J. Cleaner Prod.* **164** 58–69
[21] Ahmad R, Murtaza A F, Sher H A, Shami U T and Olalekan S 2017 *Renew. Sustain. Energy Rev.* **74** 721–32
[22] Villalva M G, Gazoli J R and Filho E R 2009 *IEEE Trans. Power Electron.* **24** 1198–208
[23] Ghasemi M A, Foroushani H M and Parniani M 2016 *IEEE Trans. Power Electron.* **31** 6281–92
[24] Gow J and Manning C 1999 *IEE Proc. - Electr. Power Appl.* **146** 193–200
[25] Pongratananukul N and Kasparis T 2004 Tool for automated simulation of solar arrays using general-purpose simulators *2004 IEEE Workshop on Computers in Power Electronics, (2004) (Proc.)* pp 10–14
[26] Nishioka K, Sakitani N, Uraoka Y and Fuyuki T 2007 *Sol. Energy Mater. Sol. Cells* **91** 1222–7
[27] Carrero C, Amador J and Arnaltes S 2007 *Renew. Energy* **32** 2579–89
[28] Ahmad G, Hussein H and El-Ghetany H 2003 *Renew. Energy* **28** 1159–68
[29] Vitorino M A, Hartmann L V, Lima A M N and Correa M B R 2007 Using the model of the solar cell for determining the maximum power point of photovoltaic systems *2007 European Conf. on Power Electronics and Applications* pp 1–10
[30] Yusof Y, Sayuti S, Abdul Latif M and Wanik M 2004 Modeling and simulation of maximum power point tracker for photovoltaic system *PECon 2004 Proc. National Power and Energy Conf., (2004)* pp 88–93
[31] Green M, Zhao J, Wang A and Wenham S 1992 *IEEE Electron Device Lett.* **13** 317–8
[32] Comsol multiphysics® (available at: https://www.comsol.com)
[33] Varshni Y 1967 *Physica* **34** 149–54